PALEONTOLOGY

Dying in the Sun: Direct evidence for elevated UV-B radiation at the end-Permian mass extinction

Feng Liu[1,2]*, Huiping Peng[1], John E. A. Marshall[3], Barry H. Lomax[4], Benjamin Bomfleur[5], Matthew S. Kent[4], Wesley T. Fraser[6], Phillip E. Jardine[5]*

Copyright © 2023 The Authors, some rights reserved; exclusive licensee American Association for the Advancement of Science. No claim to original U.S. Government Works. Distributed under a Creative Commons Attribution NonCommercial License 4.0 (CC BY-NC).

Land plants can adjust the concentration of protective ultraviolet B (UV-B)–absorbing compounds (UACs) in the outer wall of their reproductive propagules in response to ambient UV-B flux. To infer changes in UV-B radiation flux at Earth's surface during the end-Permian mass extinction, we analyze UAC abundances in ca. 800 pollen grains from an independently dated Permian-Triassic boundary section in Tibet. Our data reveal an excursion in UACs that coincide with a spike in mercury concentration and a negative carbon-isotope excursion in the latest Permian deposits, suggesting a close temporal link between large-scale volcanic eruptions, global carbon and mercury cycle perturbations, and ozone layer disruption. Because enhanced UV-B radiation can exacerbate the environmental deterioration induced by massive magmatism, ozone depletion is considered a compelling ecological driver for the terrestrial mass extinction.

INTRODUCTION

Radiometric dating using high-precision U/Pb CA-TIMS (chemical abrasion–thermal ionization mass spectrometry) on the Siberian Large Igneous Province (SLIP) and the Permian-Triassic GSSP (global stratotype section and point) at Meishan, China revealed a temporal link between SLIP and the end-Permian mass extinction (EPME) (*1*, *2*). Global warming, ocean acidification, and oceanic anoxia resulting from SLIP volcanism during the EPME have been implicated as proximate causes of marine biospheric collapse and extensive biodiversity loss (*3*–*5*). For instance, more than 80% of all marine species were extinguished (*6*) within a short time interval during an early intrusive phase of SLIP emplacement (*7*). However, how these kill mechanisms affected terrestrial ecosystems remains highly controversial (*8*, *9*).

Amidst the many potential drivers of the terrestrial EPME, enhanced solar ultraviolet B (UV-B) radiation induced by volcanism-driven ozone shield deterioration is one mechanism that can potentially impose such a devastating impact. Under this scenario, halocarbons (e.g., methyl chloride and methyl bromide) released from evaporite deposits during the Siberian Traps volcanism and sill emplacement led to ozone layer depletion (*10*, *11*). The widespread occurrence of malformed pollen grains and spores (collectively sporomorphs) during the EPME interval (Fig. 1) has been interpreted as representing increased UV-B flux, with abundant unseparated spore tetrads, pollen with aberrant numbers of apertures, and the widespread occurrence of asymmetrical, underdeveloped, or distorted sacci of pollen grains all consistent with UV-B–stimulated failures during microsporogenesis (*12*, *13*). Further, the pollen of extant *Pinus mugo* trees grown in high UV-B environments designed to simulate end-Permian ozone-depleted conditions show a range of malformation features similar to those seen in Permian bisaccate pollen (*14*). Analogous malformations in fossil spores have been taken to indicate similar ozone depletion during the end-Devonian mass extinction (*15*).

However, atmospheric pollution tied to volcanic outgassing has been proposed as an alternative causal mechanism for the frequent presence of malformed sporomorphs. Under this scenario, volcanogenic toxic pollutants—including mercury and other heavy metals and volatiles as well as acidic rain derived from SO_2 aerosols—led to environmental stress, resulting in plant physiological disorders, DNA damage, and sporomorph malformations (*16*). Volcanogenic pollution has been suggested as a mechanism for producing the malformed and dark-colored sporomorphs at the Permian-Triassic boundary (PTB) (*17*) and also severe sporomorph malformations at the Triassic-Jurassic boundary (*18*). Therefore, whether sporomorph malformations at the PTB indicate ozone depletion and increased UV-B levels at Earth's surface or instead are linked to environmental pollution is a key test to understanding the dynamics of the EPME.

Here, we address this problem using a land surface UV-B proxy based on the chemical signatures of sporomorphs. This proxy uses concentrations of UV-B–absorbing compounds (UACs) in the sporomorph outer wall (exine) to deduce past changes in ozone concentration and UV-B radiation (*19*). Plants produce UACs as a protection against the deleterious effects of UV-B, and individual plants can up-regulate UAC production in response to increasing ambient UV-B flux (*20*). The UACs in sporomorph exines are the phenolic compounds *para*-coumaric acid and ferulic acid, abundances of which can be readily detected to provide a proxy for past UV-B levels (Fig. 2). Plant UACs reflect a specific functional response to UV-B flux variations and are thus not caused by atmospheric pollution or other environmental stressors (*19*). Crucially, sporopollenin, the biopolymer that comprises the exine, has a high preservation potential in the geologic record, which has

[1]Nanjing Institute of Geology and Palaeontology, Chinese Academy of Sciences, Nanjing 210008, China. [2]State Key Laboratory of Palaeobiology and Stratigraphy and Center for Excellence in Life and Paleoenvironment, Nanjing 210008, China. [3]School of Ocean and Earth Science, University of Southampton, National Oceanography Centre, Southampton, SO14 3ZH, UK. [4]Division of Agricultural and Environmental Sciences, The School of Biosciences, The University of Nottingham, Sutton Bonington Campus, Sutton Bonington, Leicestershire, LE12 5RD, UK. [5]Palaeobotany Group, Institute of Geology and Palaeontology, University of Münster, Münster 48149, Germany. [6]Geography, School of Social Sciences, Oxford Brookes University, Oxford OX3 0BP, UK.
*Corresponding author. Email: liufeng@nigpas.ac.cn (F.L.); jardine@uni-muenster.de (P.E.J.)

Downloaded from https://www.science.org on January 18, 2023

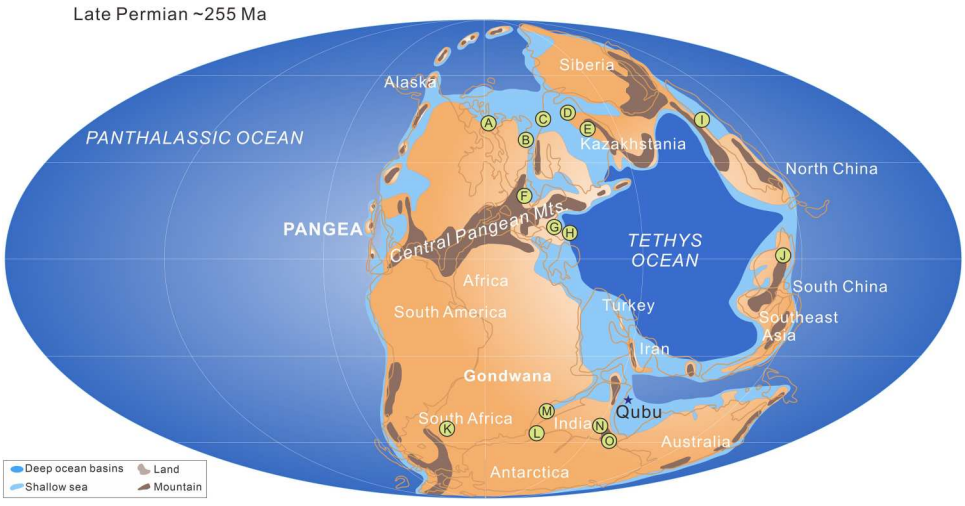

Fig. 1. Paleogeographic position of the Qubu section and Permian-Triassic palynomorph sequences featuring teratological pollen and spores [after (*12*) and (*14*) with revision]. (**A**) Sverdrup Basin, Arctic Canada. (**B**) East Greenland. (**C**) The Barents Sea. (**D**) Pechora Basin, Urals, Russia. (**E**) Russian Platform. (**F**) Ireland. (**G**) Southern Alps, Italy. (**H**) Transdanubian Mountains, Hungary. (**I**) Junggar Basin, North China. (**J**) Southwest China. (**K**) South Africa. (**L**) Sri Lanka. (**M**) Mombasa Basin, Kenya. (**N**) Auranga Basin, India. (**O**) Raniganj Basin, India.

resulted in an abundant sporomorph fossil record that extends back to the Silurian (*21*, *22*).

RESULTS

Our data come from the Qubu section in southern Tibet (28.31°N, 86.83°E). The Permian-Triassic transition in the Qubu section consists of the Changhsingian (latest Permian) Qubuerga Formation and the Induan (earliest Triassic) Kangshare Formation. Fossil conodonts, ammonoids, gastropods, and miospores recovered from the section provide precise and accurate age assessment and stratigraphic correlation (Fig. 3) (*23*). A notable negative organic and carbonate carbon-isotope excursion (CIE) in the uppermost part of the Qubuerga Formation (*24*) has been linked to the disruption of Earth's long-term carbon cycle during the EPME (*25*), which is supported by the organic carbon-isotope profile generated here (Fig. 4).

We quantified the concentrations of sporopollenin UACs using Fourier transform infrared (FTIR) microspectroscopy, a rapid, nondestructive method applicable to measuring individual sporomorphs (*26*). We scanned 1011 individuals of a single pollen–type *Alisporites* (mainly *Alisporites tenuicorpus* Balme, 1970) from 32 horizons (ca. 30 grains per horizon) of the Qubu section (Figs. 3 and 4 and data S2). This pollen type has botanical affinities with peltasperm and corystosperm seed ferns and conifers, groups that are all known to have survived the EPME (*27*). Following the removal of noisy or otherwise low-quality spectra, the dataset comprised 804 spectra (data S3), each representing one pollen grain; vetted and unvetted datasets, however, produced similar results (Fig. 5).

UAC abundances in sporopollenin have previously been estimated from FTIR spectra via the height of the wave band centered around 1510 cm^{-1}, which is associated with C═C bonds in phenolic (aromatic) functional groups, normalized against the broad OH band centered on 3300 cm^{-1} to remove the impact of sporomorph thickness on peak height measurements (Fig. 6 and data S1) (*28*). However, repolymerization of the sporopollenin biopolymer is known to take place in the geologic record, altering the sporopollenin chemical structure and decreasing the prominence of the 1510-cm^{-1} aromatic peak in FTIR spectra (*29*–*31*). Consistent with these previous findings, the FTIR spectra generated from the *Alisporites* grains studied here are substantially different from those of extant material, with larger peaks centered on 1600 cm^{-1} (C═C stretching) and 1360 cm^{-1} (symmetric CH_3 bending) and no clear 1510-cm^{-1} peak (Fig. 6). However, careful inspection of the samples across the PTB interval revealed the presence of an absorbance band centered on 1510 cm^{-1} and occurring between the 1600- and 1360-cm^{-1} peaks, consistently present but broader than the usual 1510-cm^{-1} peak (Figs. 6 and 7). Because thermal maturation and other diagenetic effects are expected to be consistent through the Qubu section, we interpret the chemical changes taking place across the PTB as reflecting changes in UAC abundances, albeit in an altered form compared to the original sporopollenin biopolymer.

Because chemical changes in the 1510-cm^{-1} region of the spectra are present as a broader band rather than a sharp peak, we measured variations in the height of this part of the spectrum in two ways: as the maximum absorbance value between 1505 and 1525 cm^{-1} [which is consistent with previous studies, e.g., (*32*, *33*)] and as the maximum absorbance value between 1450 and 1550 cm^{-1}. We also measured the heights of the 1600-cm^{-1} aromatic peak and 1360-cm^{-1} aliphatic peak to investigate their possible influence on the 1510-cm^{-1} band; in all cases, these values were divided by the height of the OH band as described above. Comparing these values shows a high concordance between the height of the 1510-cm^{-1} band, whether measured in a narrow or broad interval, and between the 1510-cm^{-1} band and the 1600-cm^{-1} peak (Fig. 8), which is expected because both represent aromatic C═C bonds. There is a much lower correlation between the height of the 1510-cm^{-1} band and the 1360-cm^{-1} peak (Fig. 8), suggesting that variations in the 1510-cm^{-1} absorbance values recorded here are not down to variations in the aliphatic component of sporopollenin and can be taken as a genuine UAC signal.

Downloaded from https://www.science.org on January 18, 2023

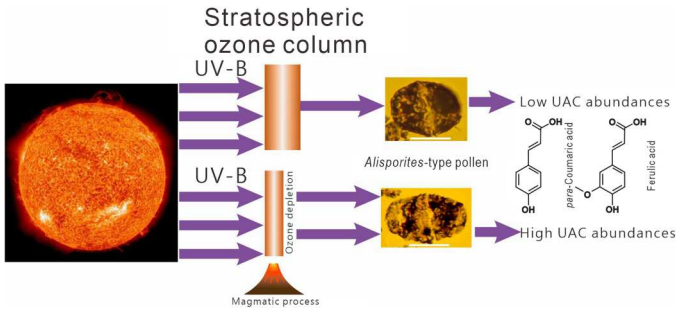

Fig. 2. Schematic representation demonstrating the magmatic process driving chemical changes within sporopollenin composition. The white scale bars in the fossil pollen image represent 20 μm.

Our data show that UAC abundances, calculated as the 1510-cm^{-1} C═C/3300-cm^{-1} OH ratio with the C═C absorbance band measured within the narrow wave number interval (see above), are stable through the Changhsingian but increase suddenly with the onset of the EPME, indicating a substantial rise in UV-B flux (Fig. 4 and Table 1). Similarly, the mercury [Hg/total organic carbon (TOC) ratio] remains constant at around 30 during the Changhsingian but increases in both raw and normalized concentration in concert with UAC abundances in the horizon 3.2 m below the PTB (Fig. 4 and Table 1). The primary source of mercury to the pre-Anthropogenic atmosphere is volcanic emissions (*34*), such that in preindustrial deposits, anomalous mercury concentration is considered a proxy for volcanic activity (*35*, *36*). From a stratigraphic standpoint, the Hg/TOC ratio peak in the Qubu section can be correlated with global anomalies of mercury concentration induced by SLIP magmatism during the EPME (Fig. 4) (*37*), although recent research suggests that coeval felsic volcanism around the Tethyan ocean and the Palaeo-Pacific margin of southern Gondwana may account for regional Hg input (*38*). In comparison, the CIE slightly lags the initial rise of UACs and mercury concentration and begins to decline 1.2 m below the PTB. Both mercury (Hg/TOC) and UAC abundances peak at the initiation of the CIE and EPME. Because the Griesbachian dolomitic limestones of the Qubu section are unsuitable for palynological analysis, UAC abundance for the 2.5 m immediately after the EPME remains unknown. However, fossil pollen spectra from overlying Dienerian deposits reveal a rapid decline in UAC abundance back to normal levels at around 500 ka after the EPME. By contrast, the mercury concentration mirrors the carbon-isotope profile with constant fluctuation through the Induan (Fig. 4 and Table 1).

DISCUSSION

The synchronicity in the anomalous UAC and mercury fluctuations with the CIE in the Qubu section are consistent with increased global UV-B radiation resulting from magmatism-derived stratospheric ozone layer deterioration, causing the widespread occurrence of malformed sporomorphs and forest sterility during the EPME (Fig. 1) (*14*). Although we found limited convincing evidence for malformations in our sporomorph record, the palynological assemblage at the EPME interval is characterized by a great abundance of amorphous organic matter (AOM), *Reduviasporonites catenulatus*, acritarchs, and rare occurrence of bisaccate pollen

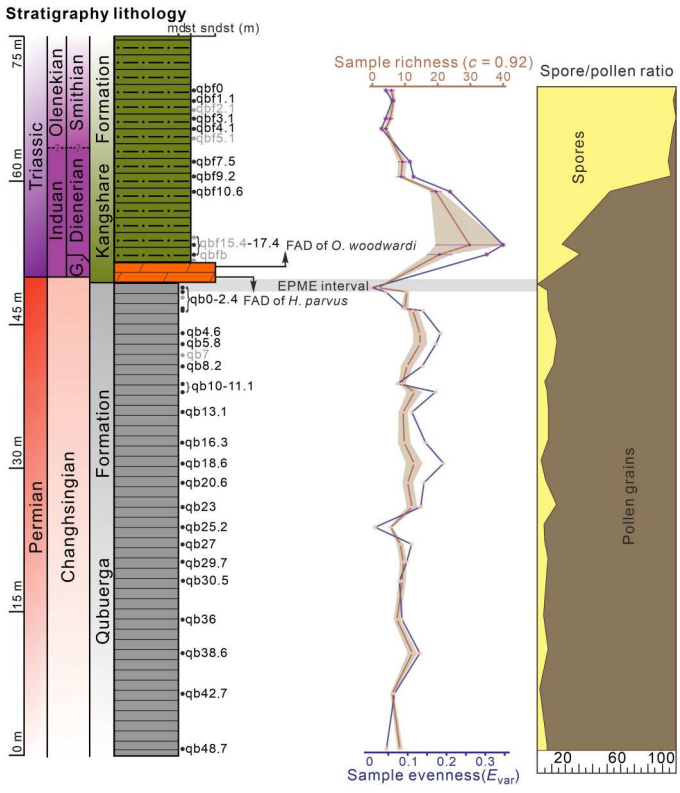

Fig. 3. Stratigraphy, rock sample location, spore/pollen ratios (*23*), and estimated sample miospore richness and evenness in the Qubu section (28.31°N, 86.83°E). The grayish sample numbers represent samples that are barren in palynomorphs. FAD represents the first appearance datum of index fossils in the section. G., Griesbachian. md, mudstone. st, siltstone. sndst(m), medium-grained sandstone. The Permian and Triassic data points are colored pink and purple, respectively.

(only *A. tenuicorpus* and *Scheuringipollenites ovatus*), in contrast to the prevalence of bisaccate pollen before the EPME (data S4 and S5) (*23*). Similar palynological turnover from bisaccate pollen- to AOM-dominated assemblages has been observed worldwide at the onset of the EPME and interpreted as a reduction in terrestrial vegetation during the EPME (*39*). However, the EPME and elevated UV-B only led to a short-term disturbance and range contraction of land plant communities, which is reflected by the rapid recovery of the palynofloral community recorded in the neighboring Griesbachian sediments in Pakistan (*40*). In the Qubu section, a rapid shift in sporomorph diversity to more even relative abundance distributions and higher within-sample richness occurred in the earliest Triassic (Fig. 3 and data S1, S4, and S5), followed by a transition to cavate trilete spore-dominated assemblages representing a lycopsid-dominated vegetation type (Fig. 3) (*23*). This substantial compositional change of palynological assemblages occurs in the Dienerian deposits (Fig. 3) and may be tied to continued SLIP volcanism and outgassing during the early Triassic (*16*). Lasting fluctuations in mercury concentrations and carbon-isotope compositions throughout the Dienerian deposits of the Qubu section (Fig. 4) also reflect the recurrent SLIP volcanism throughout about 500 ka following the EPME (*2*). However, the rapid decline of UAC values in the equivalent horizon leads us to suggest that only the liberation of volatiles by thermal alteration of organic-rich

Downloaded from https://www.science.org on January 18, 2023

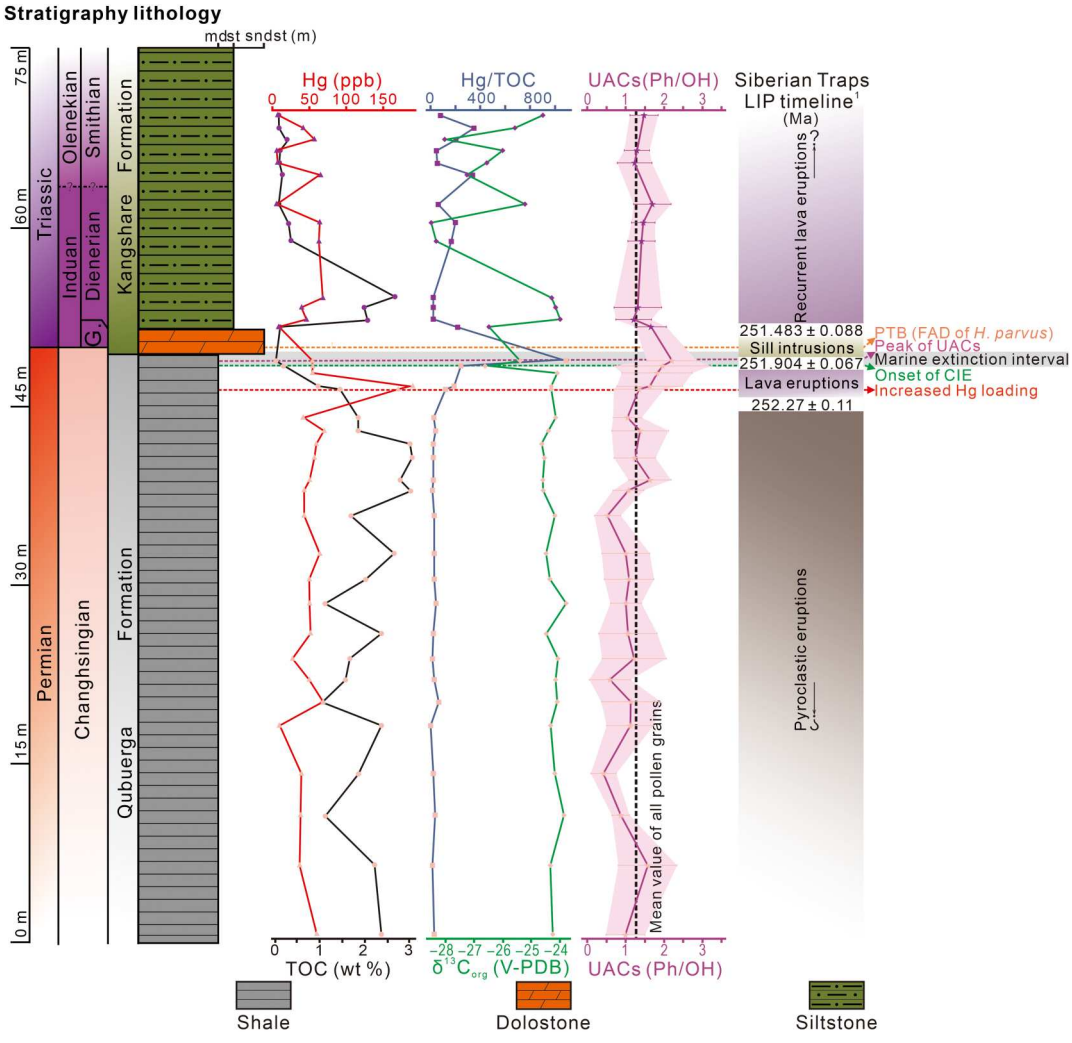

Fig. 4. Organic carbon isotope composition ($\delta^{13}C_{org}$), TOC, Hg concentration, Hg/TOC ratios, and mean UAC (Ph/OH) abundances with the shaded region showing ±1 SD about the mean in the Qubu section (28.31°N, 86.83°E), with inferred correlation to major magmatic phases of the Siberian Large Igneous Province. 1, reference (*2*). FAD represents the first appearance datum of index fossils in the section. G., Griesbachian; md, mudstone; st, siltstone; sndst(m), medium-grained sandstone; wt %, weight %. The Permian and Triassic data points are colored pink and purple, respectively. All data are given in the Supplementary Materials.

shales and evaporites could result in substantial ozone depletion and an extraordinary increase in UV-B flux (*41*).

In addition to direct, deleterious impacts on terrestrial vegetation, enhanced UV-B flux at the Earth's surface is expected to trigger cascading effects through the biosphere, with broader impacts on the carbon cycle and climate system. For example, a recent "world avoided" modeling experiment (*42*) predicted that had the Montreal Protocol not been adopted in 1987, ozone collapse and negative UV-B impacts on plant biomass would have led to a substantial decrease in the size of the terrestrial carbon sink, increasing atmospheric pCO_2 and global temperatures in addition to those forecast for the coming decades. Modeling of end-Permian ozone depletion scenarios (*11*) has predicted similar levels of ozone loss to those recreated in this counterfactual study (*42*). This suggests that the UV-B increase we have evidenced in this study was sufficiently substantial to decrease terrestrial carbon stores and contribute to atmospheric pCO_2 increases and consequent global warming, in addition to direct outgassing during SLIP emplacement and eruption, which by itself has been estimated to be too small to account for the changes in the carbon cycle during the EPME (*43*). In addition, UACs within plant tissue act as a herbivory defense by making leaves unpalatable (*44*). An increase in plant UACs, coupled with the decline in foliage nutritional value expected from elevated pCO_2 conditions (*45*), may partly explain the family-level declines in insect diversity recorded at the EPME (*46*).

A challenge with analyzing sporopollenin chemistry in deep time is the repolymerized nature of the material, meaning that we are working with a geopolymer rather than a biopolymer (*31*, *47*), and we acknowledge that we are measuring more subtle chemical variations than with extant or subfossil sporomorphs, or fossil sporomorphs from thermally immature locations. Nevertheless, we argue that detecting even subtle chemical variations across the PTB is significant, especially because the inferred increases in UACs are consistent with both empirical evidence from aberrant sporomorphs (*12*, *13*) and theoretical expectations from modeling

Downloaded from https://www.science.org on January 18, 2023

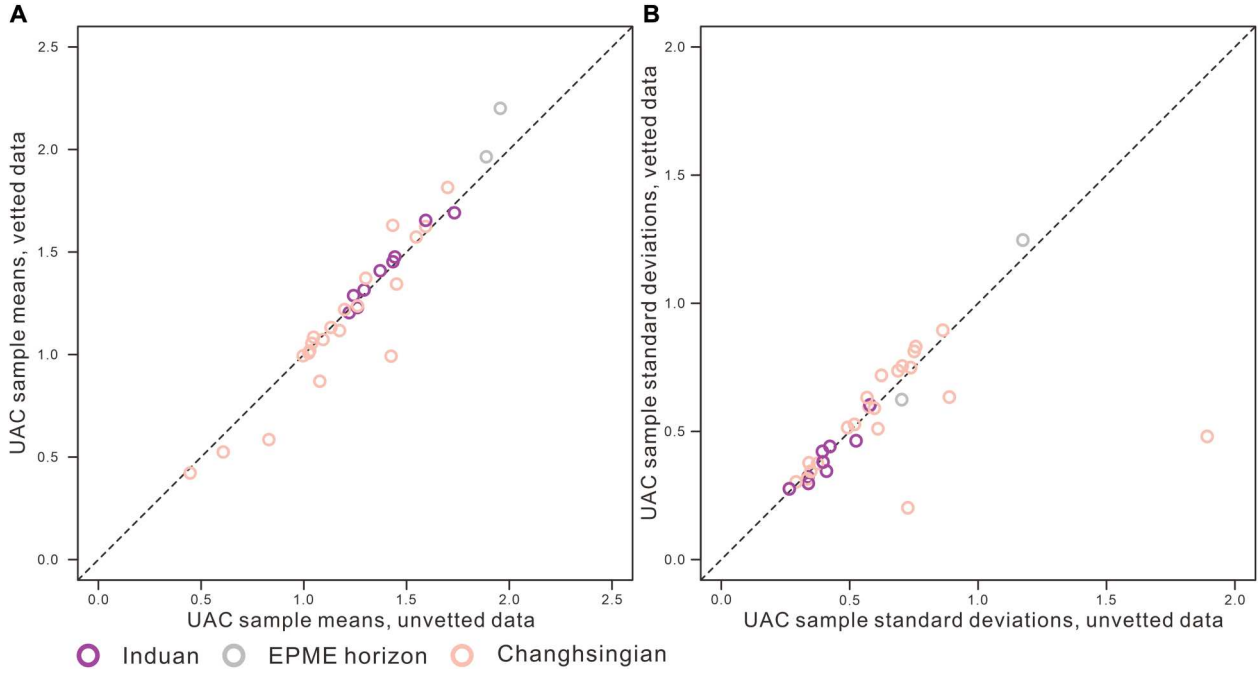

Fig. 5. Comparison of unvetted and vetted FTIR datasets. Graphs show cross-plots of UAC sample means (**A**) and UAC sample SDs (**B**) of unvetted against vetted FTIR spectra.

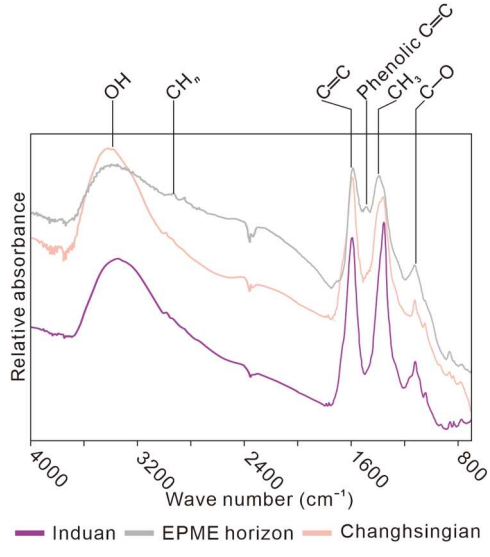

Fig. 6. Example FTIR spectra of *Alisporites*-type pollen grains recovered from the horizons below (Changhsingian), above (Induan), and the EPME.

experiments (*11*), and we have therefore interpreted these chemical shifts as providing tantalizing direct evidence for changes in UV-B flux and ozone thickness across the PTB. Further research is now needed to generate similar data from other sedimentary sections across this interval to support further the results presented here, as well as being applied to other intervals of ozone layer depletion in the geologic record. Sporomorph malformation has recently been documented for the end-Devonian and end-Triassic mass extinctions. While the former has been interpreted as a result of ozone depletion and increased UV-B flux (*15*), the latter has been attributed to toxic heavy metal pollution, particularly mercury poisoning (*18*). However, volcanism at the Triassic-Jurassic boundary is tied to the formation of the Central Atlantic Magmatic Province, with sill emplacement into Permian evaporite deposits that may have resulted in the release of ozone-destroying halocarbons in the same way as has been proposed for the EPME (*48*). Ozone depletion and increased surface UV-B flux is therefore also a plausible scenario for the end-Triassic mass extinction, and with a rich sporomorph record available, the biogeochemical methods used here provide a direct means to test this hypothesis.

MATERIALS AND METHODS

FTIR analysis

The pollen samples were processed following standard HCl-HF-HCl palynological techniques at the Nanjing Institute of Geology and Palaeontology, Chinese Academy of Sciences (*49*). However, there was no oxidation of the sporomorph material to preserve the original biogeochemical signature of the fossil sporopollenin. After maceration, 32 horizons were considered to be productive enough for FTIR analysis. The ca. 30 pollen grains of each rock sample were picked using a Nikon Eclipse inverted microscope and placed on 2-mm-thick zinc selenide discs using an Eppendorf pipette. The discs were then placed in a desiccator to allow water to evaporate at room temperature. FTIR analyses were carried out using a Shimadzu IRTracer-100 FTIR spectrometer coupled with a Shimadzu AIM 9000 microscope at Shimadzu Research Laboratory (Shanghai) Co. Ltd. Operation components were ceramic source optics, Ge-on-KBr beamsplitter and nitrogen-cooled MCT-A detector (7800 to 350 cm^{-1}). Spectra were obtained in the mid-

Downloaded from https://www.science.org on January 18, 2023

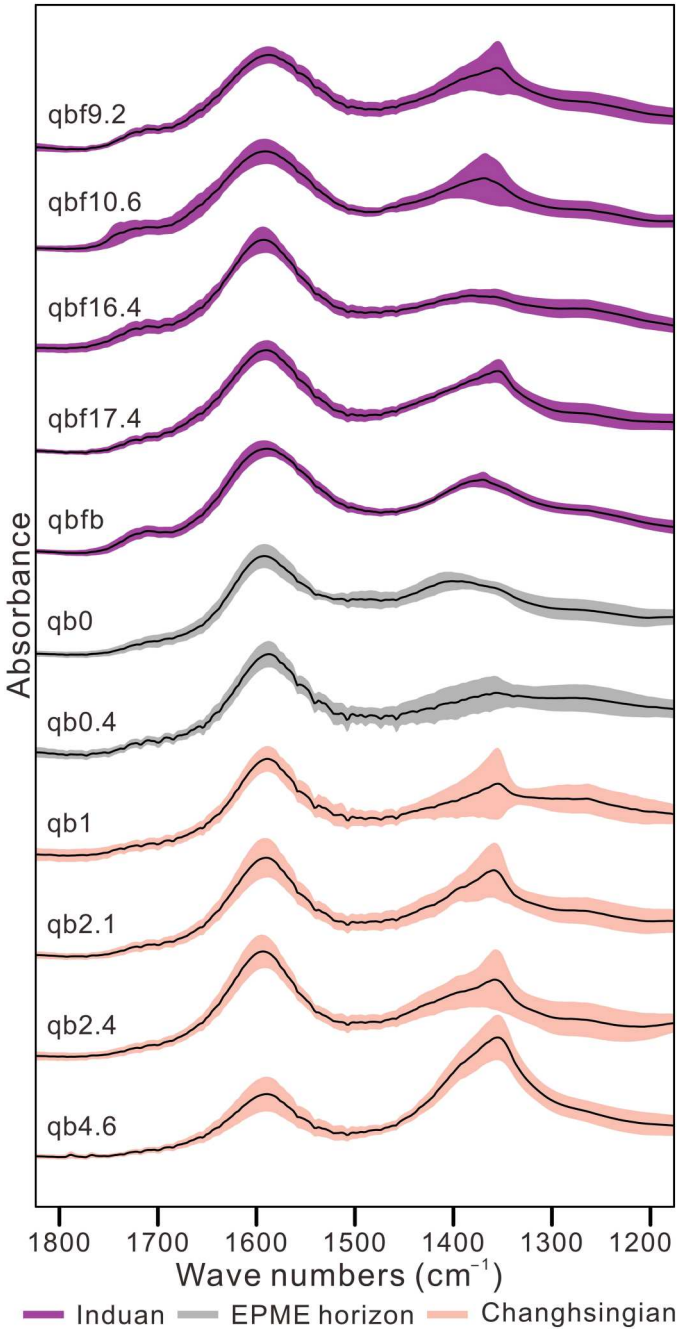

Fig. 7. Stacked FTIR spectra for samples across the PTB, showing the region between 1800 and 1200 cm^{-1}; samples are shown in stratigraphic order (oldest at the bottom, youngest at the top). Solid lines show the sample mean spectra, and shaded regions show ±1 SD.

infrared (4000 to 700 cm^{-1}) region using an aperture diameter equal to the size of pollen grains (ca. 20 × 10 μm). A 15× infrared objective was used. Two hundred scans were accumulated for each spectrum, with a spectral resolution of 2 cm^{-1}. The instrument was not purged during data acquisition, and therefore, background spectra were collected and removed immediately after every sample spectrum.

UAC concentrations were quantified by measuring the height of the 1510-cm^{-1} aromatic (stretching C═C) peak. Given that the absolute height of peaks in infrared spectra relates to the thickness of the material being scanned, the 1510-cm^{-1} peak height was therefore normalized against the broad hydroxyl (OH) peak centered on 3300 cm^{-1} (*26*, *28*, *50*, *51*). Peak heights were measured relative to a third-order polynomial baseline using R v.4.0.3 (*52*) with the package baseline v.1.3-1 (data S1 to S3) (*53*). Data vetting was carried out by excluding spectra that contained significant distortions or noise, although we note that this process had a limited impact on the results, except for lower SDs in the vetted data for some samples (Fig. 5).

TOC and carbon isotope analysis

Three-gram rock samples were cleaned and trimmed to remove visible veins and weathered surfaces and were powdered to ~200 mesh. Forty milligrams of each powdered sample was then placed into tubes and injected with phosphoric acid. The resulting gas was passed into a CO_2 coulometer to determine the percentage of carbonate in the rock sample. After multiple centrifugal, the residue was measured using an Elementar PYRO cube elemental analyzer running in carbon, nitrogen, and sulfur modeand equipped with a TCD (thermal conductivity detector), which is interfaced with an Isoprime VisION continuous flow isotope ratio mass spectrometer (IRMS). The 1- to 40-mg samples were weighed out in clean tin capsules on a Sartorius ME5 micro-balance and were then combusted at 1120°C with addition of pure oxygen. The resulting gases NO_x, SO_x, and CO_2 were subsequently reduced to N_2, SO_2, and CO_2 in the reduction column, which was held at 850°C. The elemental ratios were determined by the TCD, and the isotope ratios were determined by the IRMS. We used sulfanilamide as the C elemental standard. To normalize the isotope ratios, we used USGS40 and USGS41 as international reference materials. Values were further checked using a High Organic Sediment Standard (C 7.45%) from Elemental Microanalysis Ltd. All TOC and $\delta^{13}C_{org}$ were determined at the School of Ocean and Earth Science, University of Southampton, National Oceanography Centre, Southampton. Only one sample (qb1) had a TOC below the calibration range for Hg analysis (Table 1).

Mercury concentration measurement

Samples (0.3 g) of rock powder were weighed and placed into quartz tubes capped with ceramic fiber. Mercury concentrations were measured by combusting the tube in a Direct Mercury Analyzer (DMA-1) at the School of Ocean and Earth Science, University of Southampton, National Oceanography Centre, Southampton. Data quality was monitored via multiple analyses of the Reference Material 188-WT-L after every five samples (Table 1).

Biodiversity analysis

Within-sample richness was estimated using the coverage-based interpolation/extrapolation framework of Chao and Jost (*54*), using a coverage level of 0.92. Within-sample evenness was calculated using the E_{var} metric of Smith and Wilson (*55*), which is defined as $1 - \{2/\pi \arctan[\sum(\ln n_s - \sum \ln n_t/S)^2/S]\}$, where n_s is the number of individuals in species s, n_t is the number of individuals in species t, and S is the total number of species (data S1).

Stratigraphic correlation

The Qubu section lies near the Chinese-Nepalese border, c. 30 km north of Mt. Everest (Qomolangma). The Permian-Triassic

Downloaded from https://www.science.org on January 18, 2023

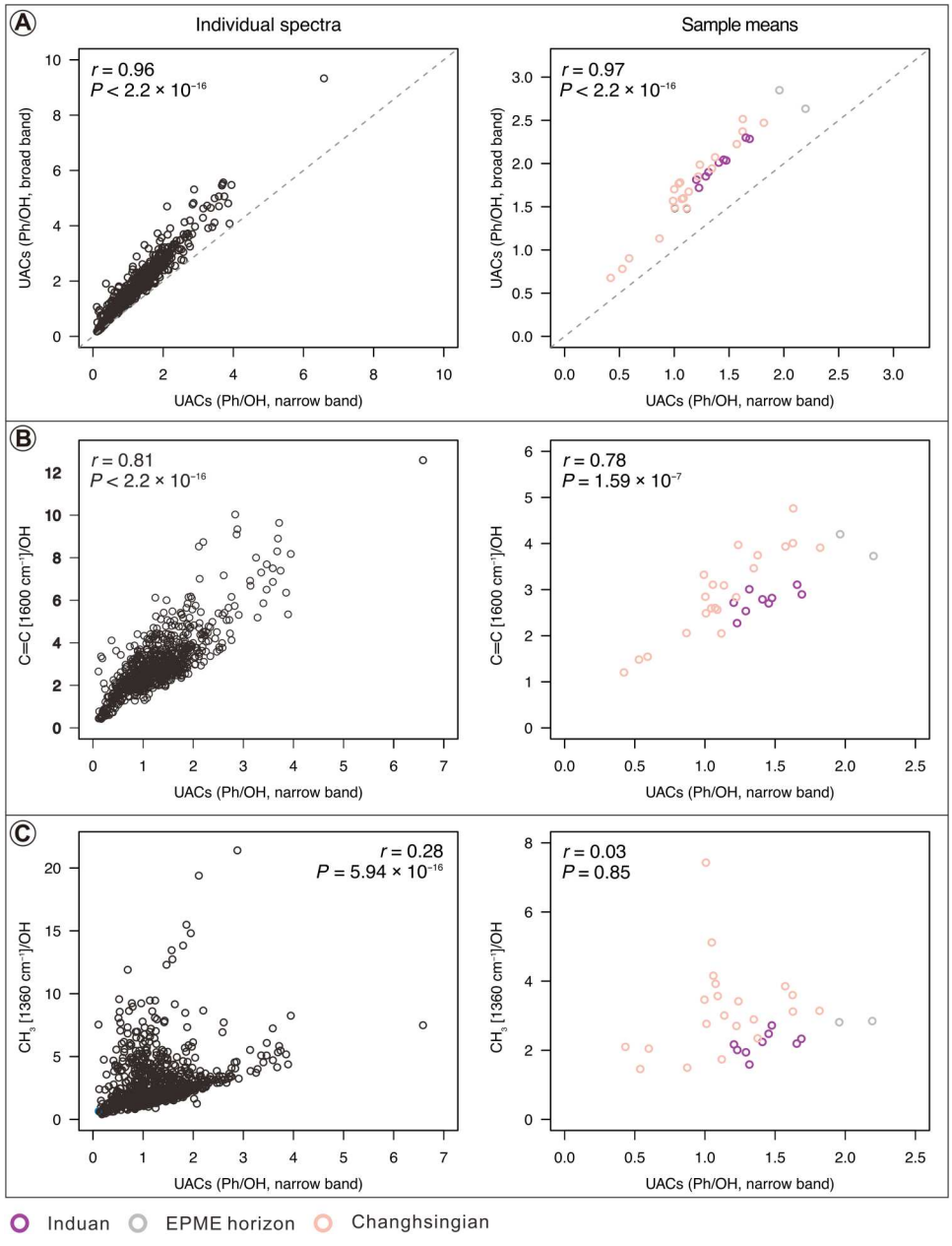

Fig. 8. Comparison of peak height ratios from the FTIR spectra, for both individual pollen grains and sample mean spectra. Graphs show the cross-correlation of narrow band C═C (1505 to 1525 cm^{-1})/OH (3300 cm^{-1}) versus broad band C═C (1450 to 1550 cm^{-1})/OH (**A**), aromatic peak (1600 cm^{-1})/OH (**B**), and aliphatic peak (1360 cm^{-1})/OH (**C**).

transition in the Qubu section consists of the Qubuerga and Kangshare formations.

The Qubuerga Formation is about 375 m thick and consists of a lower unit of bioclastic limestones and an upper unit of dark shales. The upper part (uppermost Changhsingian) of the Qubuerga Formation consists of lower, dark muddy siltstones and upper black shales overlain by a 0.5-m-thick bed of variegated shale. A *Bellerophon*-dominated gastropod fauna and some poorly preserved *Xenodiscus*-like ammonoids were recovered from the upper part of the Qubuerga Formation (*56*). These typical shallow marine fauna fossils (*57*) indicate that the upper part (latest Changhsingian) of the Qubuerga Formation was deposited in a lagoonal environment (*58*, *59*).

The lower part of the overlying Kangshare Formation in the Qubu section can be subdivided into a basal, 2.5-m-thick unit of reddish, dolomitic wackestone overlain by 17.4 m of a grayish-green silty shale unit. Abundant conodonts and ammonoids were recovered from the lower dolomitic wackestones (*24*, *59*). The first appearances of basal Triassic index fossils, including the ammonoid *Otoceras woodwardi* and the conodont *Hindeodus parvus* from the basal dolomitic wackestones of the Kangshare Formation (Fig. 3), indicate that the PTB lies no higher than 0.81 m above the basal

Downloaded from https://www.science.org on January 18, 2023

Table 1. Analytical results of TOC contents, organic carbon isotope composition, Hg concentration, and UAC abundances in the Qubu section. NA, not applicable.

Sample	Height (m)	Sample weight (TOC and $\delta^{13}C$) (mg)	Sample weight (Hg concentration) (g)	Ph/OH means (vetted data)	Ph/OH SDs (vetted data)	*n* (vetted data)	Ph/OH means (unvetted data)	Ph/OH SDs (unvetted data)	*n* (unvetted data)	$\delta^{15}N$ (Air)	$\delta^{13}C$ (V-PDB)	TON (wt %)	TOC (wt %)	Hg (ppb)	Hg/TOC
qbf0	69.6	32.493	0.3594	1.48	0.35	27	1.45	0.42	33	3.96	−24.59	0.14	0.10	8.5056936	85.0569365
qbf1.1	68.5	36.453	0.3594	NA	NA	NA	NA	NA	NA	NA	−25.58	0.13	0.12	41.932497	349.437478
qbf2.1	67.5	14.653	0.3455	NA	NA	NA	NA	NA	NA	2.05	−27.98	0.16	0.28	57.204278	204.300991
qbf3.1	66.5	33.23	0.3453	1.29	0.30	28	1.24	0.35	30	4.28	−26.00	0.12	0.13	6.000000	46.1538462
qbf4.1	65.5	38.076	0.3393	1.23	0.42	27	1.26	0.40	31	3.16	−26.56	0.12	0.13	7.4338877	57.1837513
qbf5.1	64.5	17.648	0.3432	NA	NA	NA	NA	NA	NA	3.42	−27.25	0.13	0.19	64.072329	337.222783
qbf7.5	62.1	35.4	0.3493	1.69	0.46	20	1.73	0.54	32	3.87	−25.22	0.13	0.11	7.1053826	64.5943872
qbf9.2	60.4	16.006	0.3728	1.45	0.28	33	1.44	0.28	46	4.50	−28.51	0.12	0.32	64.386437	201.207614
qbf10.6	59	15.135	0.3349	1.41	0.32	30	1.37	0.35	33	4.17	−28.33	0.15	0.38	63.019344	165.840379
qbf15.4	54.2	1.103	0.3815	NA	NA	NA	NA	NA	NA	3.98	−24.30	0.20	2.66	68.938145	25.9165958
qbf16.4	53.2	1.667	0.3626	1.31	0.60	29	1.30	0.59	31	4.29	−24.15	0.17	1.99	39.60796	19.9034975
qbf17.4	52.2	1.735	0.3801	1.20	0.44	27	1.22	0.43	30	4.35	−23.99	0.12	2.07	46.215489	22.380382
qbfb	51.2	30.665	0.3826	1.66	0.38	27	1.59	0.41	30	3.53	−26.48	0.14	0.15	32.313662	215.424414
qb0	48.7	40.268	0.3718	2.20	0.62	23	1.96	0.71	31	3.74	−25.41	0.13	0.05	54.528886	1090.57771
qb0.4	48.3	10.725	0.3749	1.96	1.24	23	1.89	1.18	30	2.30	−26.61	0.13	0.23	55.280191	240.348658
qb1	47.7	40.823	0.3316	1.82	0.89	12	1.70	0.87	33	3.23	−24.10	0.12	NA	53.7382	NA
qb2.1	46.6	2.902	0.3623	1.63	0.83	23	1.59	0.77	30	4.93	−24.31	0.18	0.99	188.69849	190.60454
qb2.4	46.3	1.934	0.3639	1.35	0.63	23	1.45	0.90	34	3.84	−24.30	0.20	1.45	170.32259	117.463857
qb4.6	44.1	1.649	0.3333	1.04	0.34	25	1.03	0.36	31	NA	−24.14	0.18	1.86	43.406927	23.3370573
qb5.8	42.9	1.246	0.3454	1.37	0.72	22	1.30	0.63	31	4.80	−24.40	0.19	1.84	69.494104	37.7685349
qb7	41.7	0.788	0.3913	NA	NA	NA	NA	NA	NA	3.71	−24.64	0.26	2.99	59.489997	19.89632
qb8.2	40.5	1.069	0.3651	1.24	0.51	31	1.27	0.50	38	4.13	−24.54	0.23	3.02	57.232266	18.9510815
qb10	38.7	1.022	0.3696	1.63	0.53	21	1.43	0.53	32	3.22	−24.59	0.25	2.80	50.32052	17.9716142
qb11.1	37.6	0.973	0.3735	1.07	0.38	24	1.09	0.35	30	3.55	−24.59	0.29	3.01	42.979286	14.2788327
qb13.1	35.6	1.63	0.376	0.53	0.31	19	0.61	0.35	30	3.14	−24.18	0.24	1.71	42.84232159	25.05398923
qb16.3	32.4	0.939	0.3593	1.00	0.59	29	1.00	0.59	30	4.51	−24.48	0.30	2.64	63.45054874	24.03429877
qb18.6	30.1	1.21	0.3392	1.09	0.63	23	1.05	0.58	30	3.97	−24.35	0.21	2.03	49.62543527	24.44602723
qb20.6	28.1	2.339	0.3532	1.01	0.37	28	1.02	0.39	33	3.08	−23.78	0.20	1.12	50.01691109	44.65795633
qb23	25.6	1.073	0.3259	1.05	0.73	26	1.04	0.70	30	4.42	−24.47	0.27	2.36	51.36452451	21.76462903
qb25.2	23.5	1.502	0.3371	1.22	0.81	27	1.20	0.76	31	5.01	−24.08	0.23	1.67	26.87357003	16.0919581
qb27	21.7	1.05	0.3599	0.59	0.51	21	0.83	0.62	30	4.09	−24.14	0.37	1.58	49.97534944	31.629968
qb29.7	19.6	2.838	0.3924	1.13	0.75	30	1.13	0.75	30	NA	−24.09	0.13	1.06	68.25603239	64.39248339
qb30.5	17.7	1.674	0.3661	1.12	0.59	24	1.18	0.61	29	4.17	−24.33	0.21	2.37	10.3537447	4.368668651

continued on next page

Downloaded from https://www.science.org on January 18, 2023

Sample	Height (m)	Sample weight (TOC and $\delta^{13}C$) (mg)	Sample weight (Hg concentration) (g)	Ph/OH means (vetted data)	Ph/OH SDs (vetted data)	*n* (vetted data)	Ph/OH means (unvetted data)	Ph/OH SDs (unvetted data)	*n* (unvetted data)	$\delta^{15}N$ (Air)	$\delta^{13}C$ (V-PDB)	TON (wt %)	TOC (wt %)	Hg (ppb)	Hg/TOC
qb36	13.7	1.581	0.3607	0.42	0.30	27	0.45	0.30	31	2.00	−24.18	0.17	1.86	38.84282789	20.8832408
qb38.6	10.1	2.757	0.3163	0.87	0.20	19	1.08	0.74	33	4.40	−23.86	0.18	1.13	37.63255836	33.30314899
qb42.7	6	1.502	0.3241	1.57	0.75	28	1.54	0.71	32	4.13	−24.34	0.23	2.21	36.61178206	16.6039828
qb48.7	0	1.223	0.3475	0.99	0.48	28	1.43	1.90	30	4.76	−24.25	0.18	2.36	60.6407876	25.69524898

Downloaded from https://www.science.org on January 18, 2023

Kangshare Formation in the Qubu section (*24*, *60*). The ammonoid *Ambites* sp. recovered from the uppermost part of the dolomitic unit suggests that the Griesbachian-Dienerian boundary is close to the upper lithological boundary of the dolomitic unit (Fig. 3) (*60*). The stable lateral distribution of the dolomitic unit and micrite and extremely small foraminiferas in the well-bedded rocks indicate low-energy deposition in a nearshore environment for the basal Kangshare Formation (*58*). Grayish-green silty shales overlying the dolomitic unit have been interpreted to be deposited in an offshore environment by facies analysis (*59*).

Our organic carbon-isotope data from the Qubu section stays around −24‰ in most Changhsingian deposits but plunges to −26‰ in the horizon 0.4 m lower than the basal boundary of Kangshare Formation (qb0.4) (Fig. 4). Although CIE here is less negative than the previous record, the negative trend of the CIE in the Qubu section is pronounced enough to be correlated with the worldwide negative CIE immediately before the EPME in context with the stable preextinction profile of $\delta^{13}C_{org}$ (Fig. 4).

Supplementary Materials

This PDF file includes:
Legends for data S1 to S5

Other Supplementary Material for this manuscript includes the following:
Data S1 to S5

REFERENCES AND NOTES

1. S. D. Burgess, S. Bowring, S.-Z. Shen, High-precision timeline for Earth's most severe extinction. *Proc. Natl. Acad. Sci. U.S.A.* **111**, 3316–3321 (2014).
2. S. D. Burgess, S. A. Bowring, High-precision geochronology confirms voluminous magmatism before, during, and after Earth's most severe extinction. *Sci. Adv.* **1**, e1500470 (2015).
3. Y. Sun, M. M. Joachimski, P. B. Wignall, C. Yan, Y. Chen, H. Jiang, L. Wang, X. Lai, Lethally hot temperatures during the Early Triassic greenhouse. *Science* **338**, 366–370 (2012).
4. M. O. Clarkson, S. A. Kasemann, R. A. Wood, T. M. Lenton, S. J. Daines, S. Richoz, F. Ohnemueller, A. Meixner, S. W. Poulton, E. T. Tipper, Ocean acidification and the Permo-Triassic mass extinction. *Science* **348**, 229–232 (2015).
5. J. L. Penn, C. Deutsch, J. L. Payne, E. A. Sperling, Temperature-dependent hypoxia explains biogeography and severity of end-Permian marine mass extinction. *Science* **362**, eaat1327 (2018).
6. J.-X. Fan, S.-X. Shen, D. H. Erwin, P. M. Sadler, N. MacLeod, Q.-M. Cheng, X.-D. Hou, J. Yang, X.-D. Wang, Y. Wang, H. Zhang, X. Chen, G.-X. Li, Y.-C. Zhang, Y.-K. Shi, D.-X. Yuan, Q. Chen, L.-N. Zhang, C. Li, Y.-Y. Zhao, A high-resolution summary of Cambrian to Early Triassic marine invertebrate biodiversity. *Science* **367**, 272–277 (2020).
7. S. D. Burgess, J. D. Muirhead, S. A. Bowring, Initial pulse of Siberian Traps sills as the trigger of the end-Permian mass extinction. *Nat. Commun.* **8**, 164 (2017).
8. R. A. Gastaldo, S. L. Kamo, J. Neveling, J. W. Geissman, M. Bamford, C. V. Looy, Is the vertebrate-defined Permian-Triassic boundary in the Karoo Basin, South Africa, the terrestrial expression of the end-Permian marine event? *Geology* **43**, 939–942 (2015).
9. H. Nowak, E. Schneebeli-Hermann, E. Kustatscher, No mass extinction for land plants at the Permian–Triassic transition. *Nat. Commun.* **10**, 384 (2019).
10. H. Svensen, S. Planke, A. G. Polozov, N. Schmidbauer, F. Corfu, Y. Y. Podladchikov, B. Jamtveit, Siberian gas venting and the end-Permian environmental crisis. *Earth and Planetary Science Letters* **277**, 490–500 (2009).
11. D. J. Beerling, M. Harfoot, B. Lomax, J. A. Pyle, The stability of the stratospheric ozone layer during the end-Permian eruption of the Siberian Traps. *Phil. Trans. R. Soc. A.* **365**, 1843–1866 (2007).
12. H. Visscher, C. V. Looy, M. E. Collinson, H. Brinkhuis, J. H. A. van Konijnenburg-van Cittert, W. M. Kürschner, M. A. Sephton, Environmental mutagenesis during the end-Permian ecological crisis. *Proc. Natl. Acad. Sci. U.S.A.* **101**, 12952–12956 (2004).
13. C. B. Foster, S. A. Afonin, Abnormal pollen grains: An outcome of deteriorating atmospheric conditions around the Permian–Triassic boundary. *J. Geol. Soc.* **162**, 653–659 (2005).
14. J. P. Benca, I. A. P. Duijnstee, C. V. Looy, UV-B–induced forest sterility: Implications of ozone shield failure in Earth's largest extinction. *Sci. Adv.* **4**, e1700618 (2018).
15. J. E. A. Marshall, J. Lakin, I. Troth, S. M. Wallace-Johnson, UV-B radiation was the Devonian-Carboniferous boundary terrestrial extinction kill mechanism. *Sci. Adv.* **6**, eaba0768 (2020).
16. D. Chu, J. D. Corso, W. Shu, H. Song, P. B. Wignall, S. E. Grasby, B. van de Schootbrugge, K. Zong, Y. Wu, J. Tong, Metal-induced stress in survivor plants following the end-Permian collapse of land ecosystems. *Geology* **49**, 657–661 (2021).
17. P. A. Hochuli, E. Schneebeli-Hermann, G. Mangerud, H. Bucher, Evidence for atmospheric pollution across the Permian-Triassic transition. *Geology* **45**, 1123–1126 (2017).
18. S. Lindström, H. Sanei, B. Van De Schootbrugge, G. K. Pedersen, C. E. Lesher, C. Tegner, C. Heunisch, K. Dybkjær, P. M. Outridge, Volcanic mercury and mutagenesis in land plants during the end-Triassic mass extinction. *Sci. Adv.* **5**, eaaw4018 (2019).
19. B. H. Lomax, W. T. Fraser, M. A. Sephton, T. V. Callaghan, S. Self, M. Harfoot, J. A. Pyle, C. H. Wellman, D. J. Beerling, Plant spore walls as a record of long-term changes in ultraviolet-B radiation. *Nat. Geosci.* **1**, 592–596 (2008).
20. H. Frohnmeyer, D. Staiger, Ultraviolet-B radiation-mediated responses in plants. Balancing damage and protection. *Plant Physiol.* **133**, 1420–1428 (2003).
21. P. Steemans, K. Lepot, C. P. Marshall, A. Le Hérissé, E. J. Javaux, FTIR characterisation of the chemical composition of Silurian miospores (cryptospores and trilete spores) from Gotland, Sweden. *Rev. Palaeobot. Palynol.* **162**, 577–590 (2010).
22. W. T. Fraser, A. C. Scott, A. E. S. Forbes, I. J. Glasspool, R. E. Plotnick, F. Kenig, B. H. Lomax, Evolutionary stasis of sporopollenin biochemistry revealed by unaltered Pennsylvanian spores. *New Phytol.* **196**, 397–401 (2012).
23. F. Liu, H. Peng, B. Bomfleur, H. Kerp, H. Zhu, S. Shen, Palynology and vegetation dynamics across the Permian–Triassic boundary in southern Tibet. *Earth-Sci. Rev.* **209**, 103278 (2020).
24. S. -Z. Shen, C.-Q. Cao, C. M. Henderson, X.-D. Wang, G.-R. Shi, Y. Wang, W. Wang, End-Permian mass extinction pattern in the northern peri-Gondwanan region. *Palaeoworld* **15**, 3–30 (2006).
25. C. Korte, H. W. Kozur, Carbon-isotope stratigraphy across the Permian–Triassic boundary: A review. *J. Asian Earth Sci.* **39**, 215–235 (2010).
26. J. S. Watson, M. A. Sephton, S. V. Sephton, S. Self, W. T. Fraser, B. H. Lomax, I. Gilmour, C. H. Wellman, D. J. Beerling, Rapid determination of spore chemistry using thermochemolysis gas chromatography-mass spectrometry and micro-Fourier transform infrared spectroscopy. *Photochem. Photobiol. Sci.* **6**, 689–694 (2007).
27. R. Potonié, Synopsis der Sporae in situ. *Beihefte zum Geologischen Jahrbuch* **52**, 204 (1962).
28. P. E. Jardine, W. T. Fraser, B. H. Lomax, M. A. Sephton, T. M. Shanahan, C. S. Miller, W. D. Gosling, Pollen and spores as biological recorders of past ultraviolet irradiance. *Sci. Rep.* **6**, 39269 (2016).
29. W. T. Fraser, J. S. Watson, M. A. Sephton, B. H. Lomax, G. Harrington, W. D. Gosling, S. Self, Changes in spore chemistry and appearance with increasing maturity. *Rev. Palaeobot. Palynol.* **201**, 41–46 (2014).
30. S. Bernard, K. Benzerara, O. Beyssac, E. Balan, G. E. Brown Jr., Evolution of the macromolecular structure of sporopollenin during thermal degradation. *Heliyon* **1**, e00034 (2015).
31. P. E. Jardine, C. Hoorn, M. A. M. Beer, N. Barbolini, A. Woutersen, G. Bogota-Angel, W. D. Gosling, W. T. Fraser, B. H. Lomax, H. Huang, M. Sciumbata, H. He, G. Dupont-Nivet, Sporopollenin chemistry and its durability in the geological record: An integration of extant and fossil chemical data across the seed plants. *Palaeontol.* **64**, 285–305 (2021).
32. P. E. Jardine, F. A. J. Abernethy, B. H. Lomax, W. D. Gosling, W. T. Fraser, Shedding light on sporopollenin chemistry, with reference to UV reconstructions. *Rev. Palaeobot. Palynol.* **238**, 1–6 (2017).
33. P. E. Jardine, W. T. Fraser, W. D. Gosling, C. N. Roberts, W. J. Eastwood, B. H. Lomax, Proxy reconstruction of ultraviolet-B irradiance at the Earth's surface, and its relationship with solar activity and ozone thickness. *The Holocene* **30**, 155–161 (2020).
34. N. E. Selin, Global biogeochemical cycling of mercury: A review. *Annu. Rev. Environ. Resour.* **34**, 43–63 (2009).
35. S. E. Grasby, B. Beauchamp, D. P. G. Bond, P. B. Wignall, H. Sanei, Mercury anomalies associated with three extinction events (Capitanian crisis, latest Permian extinction and the Smithian/Spathian extinction) in NW Pangea. *Geol. Mag.* **153**, 285–297 (2016).
36. S. E. Grasby, X. Liu, R. Yin, R. E. Ernst, Z. Chen, Toxic mercury pulses into late Permian terrestrial and marine environments. *Geology* **48**, 830–833 (2020).
37. J. Shen, J. Chen, T. J. Algeo, S. Yuan, Q. Feng, J. Yu, L. Zhou, B. O'Connell, N. J. Planavsky, Evidence for a prolonged Permian–Triassic extinction interval from global marine mercury records. *Nat. Commun.* **10**, 1563 (2019).

Downloaded from https://www.science.org on January 18, 2023

38. H. Zhang, F. Zhang, X. J.-B. Chen, D. H. Erwin, D. D. Syverson, P. Ni, M. Rampino, Z. Chi, Y.-F. Cai, L. Xiang, W.-Q. Li, S.-A. Liu, R.-C. Wang, X.-D. Wang, Z. Feng, H.-M. Li, T. Zhang, H.-M. Cai, W. Zheng, Y. Cui, X.-K. Zhu, Z.-Q. Hou, F.-Y. Wu, Y.-G. Xu, N. Planavsky, S.-Z. Shen, Felsic volcanism as a factor driving the end-Permian mass extinction. *Sci. Adv.* **7**, eabh1390 (2021).
39. C. R. Fielding, T. D. Frank, S. McLoughlin, V. Vajda, C. Mays, A. P. Tevyaw, A. Winguth, C. Winguth, R. S. Nicoll, M. Bocking, J. L. Crowley, Age and pattern of the southern high-latitude continental end-Permian extinction constrained by multiproxy analysis. *Nat. Commun.* **10**, 385 (2019).
40. E. Schneebeli-Hermann, H. Bucher, Palynostratigraphy at the Permian-Triassic boundary of the Amb section, Salt Range, Pakistan. *Palynology* **39**, 1–18 (2015).
41. J. Shen, J. Chen, T. J. Algeo, Q. Feng, J. Yu, Y.-G. Xu, G. Xu, Y. Lei, N. J. Planavsky, S. Xie, Mercury fluxes record regional volcanism in the South China craton prior to the end-Permian mass extinction. *Geology* **49**, 452–456 (2021).
42. P. J. Young, A. B. Harper, C. Huntingford, N. D. Paul, O. Morgenstern, P. A. Newman, L. D. Oman, S. Madronich, R. R. Garcia, The Montreal Protocol protects the terrestrial carbon sink. *Nature* **596**, 384–388 (2021).
43. R. A. Berner, Examination of hypotheses for the Permo–Triassic boundary extinction by carbon cycle modeling. *Proc. Natl. Acad. Sci. U.S.A.* **99**, 4172–4177 (2002).
44. S. Singh, I. Kaur, R. Kariyat, The multifunctional roles of polyphenols in plant-herbivore interactions. *Int. J. Mol. Sci.* **22**, 1442 (2021).
45. P. Stiling, T. Cornelissen, How does elevated carbon dioxide (CO_2) affect plant-herbivore interactions? A field experiment and meta-analysis of CO_2-mediated changes on plant chemistry and herbivore performance. *Glob. Change Biol.* **13**, 1823–1842 (2007).
46. S. R. Schachat, C. C. Labandeira, Are insects heading toward their first mass extinction? Distinguishing turnover from crises in their fossil record. *Ann. Entomol. Soc. Am.* **114**, 99–118 (2021).
47. J. S. Watson, W. T. Fraser, M. A. Sephton, Formation of a polyalkyl macromolecule from the hydrolysable component within sporopollenin during heating/pyrolysis experiments with *Lycopodium* spores. *J. Anal. Appl. Pyrolysis* **95**, 138–144 (2012).
48. J. H. F. L. Davies, A. Marzoli, H. Bertrand, N. Youbi, M. Ernesto, U. Schaltegger, End-Triassic mass extinction started by intrusive CAMP activity. *Nat. Commun.* **8**, 15596 (2017).
49. G. D. Wood, A. M. Gabriel, J. C. Lawson, Palynological techniques processing and microscopy, in *Palynology: Principles and Applications*, J. Jansonius, D. C. McGregor, Eds. (Publishers Press, 1996), vol. 1, pp. 29–50.
50. W. T. Fraser, M. A. Sephton, J. S. Watson, S. Self, B. H. Lomax, D. I. James, C. H. Wellman, T. V. Callaghan, D. J. Beerling, UV-B absorbing pigments in spores: Biochemical responses to shade in a high-latitude birch forest and implications for sporopollenin-based proxies of past environmental change. *Polar Res.* **30**, 8312 (2011).
51. P. E. Jardine, W. T. Fraser, B. H. Lomax, W. D. Gosling, The impact of oxidation on spore and pollen chemistry. *J. Micropalaeontol.* **34**, 139–149 (2015).
52. R Code Team, R: A language and environment for statistical computing. R Foundation for Statistical Computing (Vienna, Austria, 2020);www.R-project.org.
53. K. H. Liland, T. Almøy, B.-H. Mevik, Optimal choice of baseline correction for multivariate calibration of spectra. *Appl. Spectrosc.* **64**, 1007–1016 (2010).
54. A. Chao, L. Jost, Coverage-based rarefaction and extrapolation: Standardizing samples by completeness rather than size. *Ecology* **93**, 2533–2547 (2012).
55. B. Smith, J. B. Wilson, A consumer's guide to evenness indices. *Oikos* **76**, 70–82 (1996).
56. H.-Z. Pan, S.-Z. Shen, Late Permian (Lopingian) gastropods from the Qubuerga Formation at the Qubu section in the Mt. Everest (Qomolangma) Region, Southern Tibet (Xizang), China. *J. Paleontol.* **82**, 1038–1042 (2008).
57. H.-Z. Pan, D. H. Erwin, Gastropods from the Permian of Guangxi and Yunnan provinces, South China. *J. Paleontol.* **76**, 1–49 (2002).
58. S.-Z. Shen, C.-Q. Cao, G. R. Shi, X.-D. Wang, S.-L. Mei, Lopingian (Late Permian) stratigraphy, sedimentation and palaeobiogeography in southern Tibet. *Newsl. Stratigr.* **39**, 157–179 (2003).
59. M. Li, H. Song, A. D. Woods, X. Dai, P. B. Wignall, Facies and evolution of the carbonate factory during the Permian–Triassic crisis in South Tibet, China. *Sedimentology* **66**, 3008–3028 (2019).
60. C. Zhang, H. Bucher, S.-Z. Shen, Griesbachian and Dienerian (Early Triassic) ammonoids from Qubu in the Mt. Everest area, southern Tibet. *Palaeoworld* **26**, 650–662 (2017).

Acknowledgments: F.L. and H.P. thank F.-B. Huang (Nanjing) for help in rock sample maceration. F.L. and H.P. are grateful to J.-J. Wang from Shimadzu Research Laboratory (Shanghai) Co. Ltd. for assistance with the FTIR analysis. For mercury concentration, carbon isotope, and TOC analysis, F.L. and J.E.A.M. acknowledge P. Gaca and M. Wilding from the School of Ocean and Earth Science, University of Southampton, UK. We acknowledge the helpful comments of S. Lindström and an anonymous reviewer. **Funding:** This work was supported by National Natural Science Foundation of China grant 42172023 (to F.L. and H.P.), Second Tibetan Plateau Scientific Expedition and Research grant 2019QZKK0706 (to F.L. and H.P.), Strategic Priority Research Program (B) of the CAS grant XDB26010301 (to F.L. and H.P.), Emmy Noether Programme of the German Research Foundation grant DFG project 268272651 (to B.B.), German Research Foundation grant DFG project 443701866 (to P.E.J.), Natural Environment Research Council grant NE/R001324/1 (to M.S.K., W.T.F., and B.H.L.), and Human Frontiers Science Program grant RGP0066/2021 (to B.H.L.). **Author contributions:** Fieldwork: F.L. Methodology: F.L., P.E.J., and J.E.A.M. Investigation: H.P., F.L., P.E.J., and J.E.A.M. Writing—original draft: F.L. and P.E.J. Writing—review and editing: B.H.L., B.B., M.S.K., W.T.F., and J.E.A.M. **Competing interests:** The authors declare that they have no competing interests. **Data and materials availability:** All data needed to evaluate the conclusions in the paper are present in the paper and/or the Supplementary Materials. The FTIR spectra data for UACs analyses are provided in data S2 and S3. Count data of fossil pollen and spores for biodiversity analysis are provided in data S4 and S5. R code for the UAC measurement and palynological assemblage data analysis is provided in data S1.

Submitted 26 July 2022
Accepted 7 December 2022
Published 6 January 2023
10.1126/sciadv.abo6102

Downloaded from https://www.science.org on January 18, 2023

ScienceAdvances

Dying in the Sun: Direct evidence for elevated UV-B radiation at the end-Permian mass extinction

Feng Liu, Huiping Peng, John E.A. Marshall, Barry H. Lomax, Benjamin Bomfleur, Matthew S. Kent, Wesley T. Fraser, and Phillip E. Jardine

Sci. Adv., **9** (1), eabo6102.
DOI: 10.1126/sciadv.abo6102

View the article online
https://www.science.org/doi/10.1126/sciadv.abo6102
Permissions
https://www.science.org/help/reprints-and-permissions

Downloaded from https://www.science.org on January 18, 2023

Use of this article is subject to the Terms of service

Science Advances (ISSN) is published by the American Association for the Advancement of Science. 1200 New York Avenue NW, Washington, DC 20005. The title *Science Advances* is a registered trademark of AAAS.
Copyright © 2023 The Authors, some rights reserved; exclusive licensee American Association for the Advancement of Science. No claim to original U.S. Government Works. Distributed under a Creative Commons Attribution NonCommercial License 4.0 (CC BY-NC).